

# Large-Field Multicolor Study of Abell 168 : Subclusters, Dynamics and Luminosity Functions

Yanbin Yang<sup>1</sup>, Xu Zhou<sup>1</sup>, Qirong Yuan<sup>1,2</sup>, Zhaoji Jiang<sup>1</sup>, Jun Ma<sup>1</sup>, Hong Wu<sup>1</sup>, Jiansheng Chen<sup>1</sup>

yyb@bac.pku.edu.cn

zhouxu@bac.pku.edu.cn

## ABSTRACT

This paper presents a multicolor study of the nearby cluster of galaxies Abell 168 ( $z = 0.045$ ) with 13 intermediate-band filters in the Beijing-Arizona-Taiwan-Connecticut (BATC) filter system. After a cross-identification between the photometric data obtained from the BATC and the Sloan Digital Sky Survey (SDSS), a catalog containing 1553 galaxies down to  $r' < 20.0$  mag is achieved, which includes 121 spectroscopically confirmed member galaxies. The technique of photometric redshift has been applied to all these galaxies with combined 18-band (13 from BATC and 5 from SDSS) spectral energy distributions (SEDs), in order to perform a faint membership selection in Abell 168. As a result, 255 galaxies are newly selected as the member candidates.

Based on the enlarged sample of cluster galaxies, the spatial distribution and dynamics of Abell 168 are investigated. In the light of the spatial distribution of the member galaxies and the 0.2 – 3.5 keV X-ray image by Einstein observatory, it seems that Abell 168 consists of two merging subclusters with a relative radial velocity of  $264 \pm 142$  km s<sup>-1</sup>. With the help of ROSTAT software, a detailed investigation of the dynamics shows the intrinsic difference in the velocity distributions for these two subclusters. Under a linear two-body model, they are found to be a gravitationally bound system with 92% probability. The slight deviation of the local velocity distribution from the overall distribution in the central region may suggest a picture of head-on collision in the projection plane. By using a *double* Schechter function, the close examination of the luminosity functions reveals the different galaxy content of these two subclusters, which implies the merging process is possibly at the early stage.

---

<sup>1</sup>National Astronomical Observatories, Chinese Academy of Sciences, Beijing, 100012, P. R. China

<sup>2</sup>Department of Physics, Nanjing Normal University, NingHai Road 122, Nanjing, 210097, P. R. China

*Subject headings:* galaxies: clusters: individual (Abell 168) — galaxies: distances and redshifts — galaxies: kinematics and dynamics — galaxies: luminosity function, mass function

## 1. INTRODUCTION

The increasing volume of observational data for galaxy clusters (GCs) in multiple wavebands provides important constraints upon the formation of large scale structures and cosmology (Bahcall 1988; Dressler & Gunn 1988; Schindler 2001). The investigations on the luminosity function and the spectral features of member galaxies in a rich cluster will help us to understand not only the structures and dynamics of the whole galaxy cluster but also the formation and evolution of galaxies under such a dense environment (Dressler 1984; Poggianti 2002).

Spectroscopic observation in the optical band is still the most straightforward and powerful approach to the membership determination. However, the reliable spectroscopies for the faint galaxies in a cluster is still an unattainable goal for the large telescopes. With the development of photometric redshift technique, the redshifts of faint galaxies can be significantly determined according to their SEDs. The BATC sky survey is specially designed for this purpose. In this paper we present a large-field multicolor study of the galaxy cluster Abell 168 based on the BATC observations with 13 intermediate-band filters, which covers the whole optical band. Improvement of the accuracy in photometric redshift estimate with our multicolor system allows us to study the spatial and the dynamic properties of the nearby clusters of galaxies (Yuan et al. 2001; Yuan et al. 2003).

Abell 168 is a nearby ( $z = 0.045$ ) cluster of galaxies located at  $01^{\text{h}}15^{\text{m}}10^{\text{s}}.2 +00^{\circ}12'18''$  (J2000.0) with richness of II–III (BM classification). Its distance module is 36.45 by assuming  $q_0 = 0.5$  and  $H_0 = 75 \text{ km s}^{-1} \text{ Mpc}^{-1}$  (also used throughout this paper). The luminosity function of Abell 168 was remarked as the best example of non-Schechter form by Dressler (1978), which was confirmed by Oegerle, Ernst & Hoessel (1986). Based on the positional discrepancy of  $\sim 10'$  (i.e.,  $\sim 540 \text{ kpc}$ ) between the X-ray and the optical center, Ulmer, Wirth & Kowalski (1992) suggested that Abell 168 was formed by the collision of two clusters with approximately equivalent sizes. It is reported that the X-ray emission of Abell 168 has two peaks with surface brightness of  $9 \times 10^{-14}$  and  $3 \times 10^{-14} \text{ erg s}^{-1} \text{ cm}^{-2}$ , respectively (Tomita et al. 1996). They supposed that the star-forming processes will be triggered when gas-rich galaxies rush into the higher density regions. However, Tomita et al. (1996) failed to find the enhanced fraction of blue galaxies in the region between these two X-ray peaks.

This paper aims at not only selecting faint member galaxies of Abell 168 by photometric

redshift technique, but also investigating the substructures in the spatial distribution and the line-of-sight velocity distributions. We wish to provide the direct evidence of the ongoing merge event of Abell 168 from our analysis of multicolor photometries. This paper is structured as follows: In §2, we describe the BATC observations, the data reduction. The technique of photometric redshift is used to estimate the redshift for all galaxies, then the membership selection of Abell 168 is performed. In §3, the substructures of Abell 168 are explored on the basis of the member galaxy distribution and the X-ray emission of hot gas. The dynamics of substructures is also studied. In §4 the luminosity functions (LFs) of Abell 168 are analyzed. The summary is given in §5.

## 2. DATA

### 2.1. BATC Observation and Data Reduction

The BATC program is a large-field ( $58' \times 58'$ ) multicolor sky survey based on the 60/90 cm f/3 Schmidt Telescope of National Astronomical Observatories, Chinese Academy of Sciences (NAOC). A Ford Aerospace 2048 $\times$ 2048 CCD camera with the pixel size of  $15 \mu\text{m}$  ( $\sim 1''.7/\text{pixel}$ ) is mounted on the telescope. The BATC filter system contains 15 intermediate-band filters (Fig. 1) covering a wavelength range from 3000 to 10 000 Å, which are specifically designed for avoiding night sky emission lines. A detailed description of the BATC photometric system can be found in Fan et al. (1996) and Zhou et al. (2003).

Fig. 1: Transmission of filters.

From August 1995 to March 2002, we totally accumulated about 37 hours exposure for Abell 168 with 13 filters. More information about our observations is given in Table 1. The raw data are processed with an automatic data reduction software named PIPELINE I (Fan et al. 1996) which includes the bias subtraction and the dome flat-field correction. The technique of integral pixel shifting is used in the image combination during which the cosmic rays and bad pixels are corrected by comparing multiple images. The mean error of position calibration is  $\sim 0''.5$  by taking the Guide Star Catalog (GSC) as standard. By using the PIPELINE II software (Zhou et al. 2003), developed on the basis of the DAOPHOT kernel, photometries are performed for all the objects detected. As a result, the photometries with the Point Spread Function (PSF) model and the different apertures are obtained for 4798 objects detected in at least 3 bands. The flux calibration of the SEDs is performed by using the Oke-Gunn standard stars which were observed during photometric nights. The detailed information about calibration can be found in Zhou et al. (2001). Because we have no calibration image for  $g$  filter, we instead perform a model calibration that is developed specially for the large-field photometric system by Zhou et al. (1999).

Table. 1: The statistics of observations.

## 2.2. Combining the BATC and the SDSS SEDs of galaxies

Abell 168 has been observed by SDSS with five broad bands, namely  $u', g', r', i', z'$  (Fig. 1), and the photometric data are distributed in the SDSS Early Data Release (EDR, see Stoughton et al. 2002). The method of combining the SDSS photometric data and the BATC SEDs is explored recently by Yuan et al. (2003), and this work shows that the combined SEDs could lead to a more accurate estimate of photometric redshifts. We cross identify the BATC source list with the SDSS photometric catalog in the same region, and a catalog containing 2580 galaxies and 2218 stars is achieved. The object classifications are taken from the result of SDSS photometries. For the photometries of BATC, we adopt the PSF magnitudes for stars, and take a fixed aperture with a radius of 4 pixels (i.e.,  $r_{\text{ap}} \sim 6''.8$ ) for galaxies. In order to combine the photometric results of the BATC and the SDSS, an aperture-correction should be applied to the SDSS model magnitudes ( $m_{\text{model}}$ ) by

$$\Delta m = m_{\text{ap}} - m_{\text{model}} = -2.5 \log \frac{\int_0^{r_{\text{ap}}} 2\pi r I(r) dr}{\int_0^{\infty} 2\pi r I(r) dr}, \quad (1)$$

where  $m_{\text{ap}}$  is the aperture magnitude,  $I(r)$  is the preferred profile function of surface intensity (e.g., the power law or de Vaucouleurs  $r^{1/4}$  model). The model magnitude in each band and its corresponding parameters that are used to quantify the preferred brightness profile can be found in the SDSS data.

To observe the possible systematic offset between the BATC and the SDSS photometric system, we derive the zero point difference of SED (ZPDS) for each object by calculating the difference between the SDSS  $r'$  magnitude and the interpolated BATC magnitude at 6180Å. Fig. 2 shows the distribution of ZPDSs for all the objects detected. For stars, the magnitude offset between these two photometric systems approximates to zero, indicating that the BATC and SDSS photometric systems are in good agreement. For galaxies, a more widely spread distribution of ZPDSs is found. This might be the result from the errors in photometries and the uncertainties in model fittings. For adapting to BATC multicolor photometric system, the SDSS SEDs are corrected by adding their ZPDS. Finally, we obtain the combined SEDs, including 13 BATC bands plus 5 SDSS bands, for 1553 galaxies brighter than  $r' = 20$  mag.

Fig. 2: Zero point distribution.

## 2.3. Photometric Redshift and Membership Determination

The photometric redshift technique was originally developed for detecting the high- $z$  objects based on the broad-band photometries (Pelló et al. 1999; Bolzonella, Miralles, & Pelló 2000). The 15-intermediate-band SEDs obtained by the BATC photometric system can be regarded as the rough spectrum. The advantages of the BATC data in measuring the photometric

redshift of some faint galaxies can be expected. With the BATC SEDs (Yuan et al. 2001, Xia et al. 2002) and the combined SEDs of the BATC and the SDSS (Yuan et al. 2003), the photometric redshifts of faint galaxies can be estimated with a certain accuracy ( $\Delta z_{\text{phot}} \approx 0.02$ ), which allows us to isolate the member galaxies for some nearby galaxy clusters.

The technique of photometric redshift has been applied to the 18-band SEDs with the help of the *Hyperz* code (Bolzonella, Miralles, & Pelló 2000). The red-shifted spectral templates of normal galaxies are used to fit the observed SEDs, and the reddening law is set to be a free parameter during the fitting. The photometric redshift for each galaxy is searched in a redshift range from 0.0 to 1.0, with a searching step of 0.005. The histogram of  $z_{\text{phot}}$  for all galaxies is plotted in Fig. 3, and most of them are located at  $z < 0.5$ . 195 galaxies with known spectroscopic redshifts  $z_{\text{spec}} < 0.25$  are selected to derive the uncertainty of photometric redshift which is found to be  $\sim 0.024$  (see Fig. 4).

Fig. 3: The histogram of photometric redshift.

Fig. 4: A comparison of photometric redshifts and spectroscopic redshifts.

According to the known spectroscopic redshifts, there are 121 galaxies distributed in a range from 0.04 to 0.05. We take them as the member galaxies of Abell 168. About 90% (109/121) galaxies have photometric redshifts within the range  $[0.02, 0.07]$ , thus we take this range as the criterion for the membership determination based on the photometric redshift. As a result, 255 galaxies are selected as the member candidates. Together with the spectroscopically confirmed members, we totally obtain an enlarged sample of 376 member galaxies. It should be noted that the uncertainty of photometric redshift is rather large compared with the intrinsic dispersion of Abell 168, but it still can be used to select the member galaxy candidates with high efficiency, especially for the faint galaxies.

### 3. SUBSTRUCTURES

#### 3.1. Spatial Distribution of Members and X-ray Map

Fig. 5 gives the spatial distribution of 376 member galaxies (small circles), with its corresponding contour map (thin lines) of the number density superposed. In the figure, D indicates the density peak located at  $01^{\text{h}}15^{\text{m}}06^{\text{s}} +00^{\circ}19'12''$  (J2000.0). The spatial distribution is elongated along the NW-SE direction with a position angle of  $\sim 30^{\circ}$ . A possible group (A168WG), indicated by E in the figure, can be recognized to the west of the cluster core. The group is close to the high density region and seems to be falling down to the center, increasing the galaxy density there. A similar spatial distribution was earlier derived by Kriessler & Beers (1997), but their sample of 106 galaxies did not show the core structures and the group clearly. We take the density peak as the center, and then derive the radial number density profile in Fig. 6.

It is clear that most of the galaxies concentrate within a range of about  $12'$  ( $\sim 0.7$  Mpc).

Fig. 5: The member distribution and the X-ray map.

Fig. 6: The number density profile.

The X-ray image in  $0.2 - 3.5$  keV band, observed by IPC of Einstein Observatory, is overlaid on the spatial distribution in Fig. 5 (thick lines). It is interesting that the X-ray map and the member distribution coincide well with each other both in their spatial locations and their shapes. As mentioned above (§1), the X-ray emission of Abell 168 has two peaks, marked by A and B in Fig. 5. The higher X-ray peak, point A, is located at  $01^{\text{h}}14^{\text{m}}57^{\text{s}} +00^{\circ}25'04''$  (J2000.0) with a distance of  $\sim 6'$  (i.e.,  $\sim 320$  kpc) to the density peak. In the figure, C points to the cD galaxy UGC 00797. Point A is very close to the cD, which agrees with the traditional experience that D/cD galaxies are located around the peak of the X-ray emission (Jones et al. 1979; Forman & Jones 1982). However, this cD galaxy significantly deviates from the local density peak of Abell 168, which seems inconsistent with the idea that a D/cD appears to be associated with the center of its host cluster (Beers & Geller 1983; Oegerle & Hill 2001). On the other hand, the lower X-ray peak, point B, is surrounded by the clustering bright galaxies. From the shape of the X-ray emission, the hot gas between the two peaks seems to be pushed away from the center by the head-on collision of the two clumps. Combining all above characteristics, it seems that there are some substructures in Abell 168. Ulmer, Wirth & Kowalski (1992) pointed out that Abell 168 was possibly formed by the collision of two subclusters. If this is true, it is reasonable to assume the collision occurs along the elongated direction. To explore the substructures in detail, we artificially divide the main region of Abell 168 (indicated by a  $0.4^{\circ} \times 0.6^{\circ}$  box in Fig. 5) into two equal parts. One is centered at the higher X-ray peak with 79 galaxies. We call it north subcluster (A168N). Another is located at the lower X-ray peak with 97 galaxies, named south subcluster (A168S). In the following sections we try to find other evidences to support that they are indeed physically different parts in Abell 168, in other words, they are really two subclusters, and we will show that they seem to be under a merging process.

### 3.2. Dynamics of Substructures

Provided Abell 168 is formed by merging of two subclusters, the dynamics remaining after the collision should be presented by testing the velocity distribution. On the basis of the spectroscopically confirmed member galaxies, we are allowed to study the dynamics of Abell 168 in detail. The statistical parameters of A168N, A168S, A168WG and A168 are listed in Table 2. The mean redshift ( $z$ ), the mean velocity ( $v_r$ ) and the velocity dispersion ( $\sigma_r$ ) are all calculated by the biweight statistic in ROSTAT software (Beers, Flynn, & Gebhardt 1990), except the velocity dispersion of A168WG is taken from the gapping statistic. The asymmetry

index (AI) and the tail index (TI) of the velocity distributions are also provided by ROSTAT. Fig. 7 shows the velocity distribution of these two subclusters, respectively. The distribution of A168N is more concentrated than that of A168S. It seems that, for A168S, there is a gap at  $\sim 13\,000\text{ km s}^{-1}$ , which can be clearly seen from a stripe density plot in Fig. 8. According to the value of TI (see Bird & Beers 1993 for detail), A168N possesses a light-tailed distribution, while the distribution of A168S is near Gaussian. This suggests that these two distributions are intrinsically different. Moreover, the classical K-S test also shows the velocity distributions of these two subclusters are from the different parent distributions with 94% probability.

Fig. 7:  $V_r$  distribution of A168N and A168S.

Fig. 8: Stripe density plot.

Although it appears the obvious interaction between these two subcluster according to the spatial distribution, one should keep in mind this is a projection effect. So it is necessary to estimate the probability that they are gravitationally bound, in order to confirm they are really two interacting subclusters. We take a linear two-body model for the system as Beers, Geller, & Huchra (1982) did in analyzing the cluster Abell 98. Under this model, the relative velocity  $V$  and the separation  $R$  between two subclusters can be converted to the observational quantities: the relative radial velocity  $V_r = V \sin \alpha$  and the projection separation  $R_p = R \cos \alpha$ . The projection angle  $\alpha$  ( $\in [0, \pi/2]$ ) is defined as the angle between the line connecting the two subclusters and the plane of sky. The energy relation for gravitational binding is taken from the Newtonian criterion

$$\frac{V_r^2 R_p}{2GM} \leq \sin^2 \alpha \cos \alpha, \quad (2)$$

where  $G$  is the gravitational constant.  $M$  is the system mass, equal to the total mass of the two subclusters. The difference of mean velocity between A168N and A168S can be easily figured out  $V_r = 264 \pm 142\text{ km s}^{-1}$ . We take  $R_p = 0.584\text{ Mpc}$ , the distance between the two X-ray peaks which roughly represent the centers of these two subclusters. Following the method described in Beers, Geller, & Huchra (1982), the mass and the gravitational scale lengths of A168N, A168S and A168 are estimated and listed in Table 2. The probability of gravitational binding can be obtained by the formula

$$P = \frac{1}{A} \int_0^{+\infty} p(V_r) p(\alpha|V_r) dV_r, \quad (3)$$

where  $A$  is re-normalization factor.  $p(V_r)$  is the probability distribution of the velocity which is assumed to be a Gaussian.  $p(\alpha|V_r)$ , which can be obtained from Eq. 2, is the probability of the valid  $\alpha$  for gravitational binding at a given  $V_r$ . Integration is over all the appropriate values of velocity. As the results, we find these two subclusters are gravitationally bound with a probability of 92%.

Another efficient statistic method to test the substructures of the radial velocity distribution was recently introduced by Colless & Dunn (1996), who keep the spirit of Dressler-

Shectman test (Dressler & Shectman 1988) and employ the standard K-S test to compare the velocity distribution of the local group,  $n$  nearest neighbors, and the whole velocity distribution. The statistic is defined as

$$\kappa_n = \sum_{i=1}^N -\log [P_{\text{KS}}(D > D_{\text{obs}})], \quad (4)$$

where  $N$  is the number of all member galaxies of a cluster, and  $D$  is the statistic in standard K-S test. For each galaxy, we compute the probability,  $P_{\text{KS}}(D > D_{\text{obs}})$ , of its local group via Monte Carlo simulation by randomly shuffling velocities every time. This probability gives the an indication of how significant the observed  $D_{\text{obs}}$  is by comparing with the simulations.  $\kappa_n$  is an indication that the local velocity is different from the overall distribution.

We take the group size of  $n = 10$ . By involving  $10^5$  simulations, we find that  $\kappa_{10} = 0.000\%$ , almost no simulated  $D$  greater than the observed  $D_{\text{obs}}$ . A significant deviation of local velocity distribution from the overall distribution can be found in Fig. 9. The bubble radius for each galaxy is proportional to  $-\log [P_{\text{KS}}(D > D_{\text{obs}})]$ . Consistent with the result of spectroscopic redshifts, no further substructure was found in the central region, because the photometric redshift is not precise enough to distinguish the small difference, such as  $\sim 260 \text{ km s}^{-1}$ , in velocity. The result possibly suggests that the two subclusters are approaching each other along the plane perpendicular to our line of sight. The obvious bubble concentration at the west possibly supports the existence of the west group discussed in the section §3.1.

Fig. 9: Bubble plot.

## 4. LUMINOSITY FUNCTIONS

### 4.1. Double Schechter Function

The luminosity function is a key diagnostics for clusters of galaxies because it is tightly related to the dynamical evolution and the merging history of galaxy clusters. In the past decades, the LFs of GCs are well described by the famous Schechter function, which was originally proposed by Schechter (1976):

$$\phi(L)dL = \phi^* (L/L^*)^\alpha \exp(-L/L^*) d(L/L^*), \quad (5)$$

where  $\phi^*, L^*, \alpha$  are the normalization parameter, the characteristic luminosity and the faint slope parameter, respectively.

Recently, the deep observation of the Coma cluster reveals their LFs possess an enhanced faint tail (e.g., Trentham & Tully 2002). It is widely perceived that a single Schechter function gives a poor representation of the data when the LFs extend to the fainter end (Biviano et al. 1995; Durret, Gerbal, Lobo & Pichon 1999; Trentham & Tully 2002). The segregation in

LFs of GCs suggests that there are at least two populations of the galaxies in clusters (Durret, Adami & Lobo 2002). For example, Ferguson & Sandage (1991) take a form of Gaussian part plus Schechter function in order to probe the two populations, the giants and the dwarfs.

The Schechter function works well for the bright end as shown in the previous literatures, such as Dressler (1978), Paolillo et al. (2001). However, the present extending LFs require a variation to describe the enhanced tail rather than a single Schechter function. Hence we propose an acceptable *double* Schechter function (DSF hereafter).

$$N(M) = \phi_0^* [10^{-0.4(M-M_0^*)}]^{\alpha_0} e^{10^{-0.4(M-M_0^*)}} + \phi_1^* [10^{-0.4(M-M_1^*)}]^{\alpha_1} e^{10^{-0.4(M-M_1^*)}}. \quad (6)$$

Each term has the same form as the Schechter function in Eq. 5.  $M_i^*$  ( $i = 0, 1$ ) is the characteristic absolute magnitude with an equivalent characteristic luminosity;  $\phi_i^*, \alpha_i$ , ( $i = 0, 1$ ) have the same meanings as in Eq. 5.

## 4.2. Luminosity Functions

We use DSF to fit the observed LFs by means of the  $\chi^2$  minimization. The results are listed in Table 3 and plotted in Fig. 10. A168S shows a decay tail while A168N shows an increasing one, suggesting that the galaxy contents of these two regions are quite different. We also compute the ratio of bright galaxies ( $M_{r'} \leq -18.5$ ) to the faint ( $M_{r'} > -18.5$ ) for these two subclusters. This ratio for A168N is found to be 32/47=0.68. However, for A168S, the ratio is 56/41=1.37. It is obvious that the bright galaxies are more abundant in A168S while the faint galaxies prefer to occur in A168N. This can be interpreted by the cannibalism model (Hausman & Ostriker 1978). That is to say: the cDs are likely to be formed by accreting the surrounding massive galaxies, which naturally results in the deficit of bright galaxies in the most dynamically evolved clusters (Lugger 1986). Hence, the formation and evolution of these two subclusters might be different. A168N, associated with the cD galaxy UGC 00797, is likely to be more evolved than A168S. To confirm our dividing of A168N and A168S is not accidental. We try other methods of dividing the core region. For example, we divide the core region into an east and a west part equally along the elongated direction of the spatial distribution. In this case, the clear contrast in the LFs disappears, which supports the dividing of A168N and A168S is a special choice, and they are the two subclusters under the merging event of Abell 168.

Table. 2: The fitting results of LFs of Abell 168.
--

Fig. 10: The observed luminosity functions are fitted by DSF.
---

Panel (c) in Fig. 10 shows the LF of the central region (A168N+S) of the cluster. As shown in previous works of Dressler (1978) and Oegerle, Ernst, & Hoessel (1986), the LF has a quite

flat tail which is, however, an average of LFs of A168N and A168S according to the present work. As for the whole field, the observed LF and its fitting model are shown in panel (d) of Fig. 10. For the overall LF, DSF gives a good description to the obvious enhanced faint tail at  $M_{r'} > -18.5$  mag. Compared with the LF of the central region, the overall LF suggests that the faint galaxies (possible dwarfs) tend to be located in the outer region of the cluster. This perhaps support the population-density relation: dwarfs are more common in lower density environments (Phillipps, Driver, Couch, & Smith 1998).

## 5. SUMMARY

We accumulated about 37 hours of high quality observations of Abell 168 with 13 intermediate filters of BATC photometric system. In the EDR of SDSS, we find that the photometry and the spectroscopic redshift measurement are completed in the same field. After a cross-identification with SDSS, we combine the photometric data of the objects detected in two systems getting the 18-band SEDs, which include 13 BATC bands and 5 SDSS bands. A complete sample of 1553 galaxies brighter than  $r' = 20$  mag is achieved for the subsequent study.

By using the technique of photometric redshift, we get an enlarged sample of 376 galaxies, including 121 spectroscopically identified member galaxies and 255 newly selected member candidates. Spatially, the member galaxies show an elongated distribution along the NW-SE direction with a position angle of  $\sim 30^\circ$ , which is consistent with the spatial characteristic of the X-ray image obtained by Einstein Observatory. Moreover, the two X-ray peaks and the deviation of the cD galaxy UGC 00797 from the local density peak support the existence of substructures in Abell 168. According to the spatial characteristics, we artificially divide the core region into two parts, A168N and A168S. By employing ROSTAT software, a detailed investigation of the dynamics of these two subclusters is performed. A relative radial velocity of  $264 \pm 142$  km s $^{-1}$  was found between them. Their velocity distributions are intrinsically different and should be from the different parent distributions. Via building a linear two-body model, they are found to be gravitationally bound with a probability of 92%. Investigation of LFs by the DSF shows an obvious difference in the galaxy content of these two subclusters. The A168S is dominated by bright galaxies while A168N has larger number of faint galaxies. A168N is a sub-system associated with the cD galaxy and likely to be a more evolved system than A168S. All these indications are consistent and support that Abell 168 is likely to be a head-on merging system at its early stage of the process, and that the collision plausibly occurs along the direction perpendicular to our line of sight.

The authors would like to thank the referee Timothy Beers who gives the good suggestions to improve the paper. We are grateful to the following persons for their valuable suggestions and

discussion: Dr. HaiGuang Xu, SuiJian Xue, XiangPing Wu, XiaoFeng Wang, Yu Liu, ZhengYu Wu, Mr. Yu Lu, Ms. Bin Yang, LiFang Xia, and especially Mr. Albrecht Rüdiger. We also appreciate the assistants who contributed their hard work to the observations. This research has made use of the NASA/IPAC Extragalactic Database (NED), the EDR of SDSS, High Energy Astrophysics Science Archive Research Center (HEASARC). This work is supported by the National Key Base Sciences Research Foundation (NKBRSF, TG199075402) and is also supported by the Chinese National Science Foundation (NSFC).

## REFERENCES

- Bahcall, N. A. 1988, ARA&A, 26, 631
- Beers, T. C., Geller, M. J., & Huchra, J. P. 1982, ApJ, 257, 23
- Beers, T. C. & Geller, M. J. 1983, ApJ, 274, 491
- Beers, T. C., Flynn, K., & Gebhardt, K. 1990, AJ, 100, 32
- Bird, C. M. & Beers, T. C. 1993, AJ, 105, 1596
- Biviano, A., Durret, F., Gerbal, D., Le Fevre, O., Lobo, C., Mazure, A., & Slezak, E. 1995, A&A, 297, 610
- Bolzonella, M., Miralles, J.-M. & Pelló, R. 2000, A&A, 363, 476
- Colless, M. & Dunn, A. M. 1996, ApJ, 458, 435
- Dressler, A. 1978, ApJ, 223, 765
- Dressler, A. 1984, ARA&A, 22, 185
- Dressler, A. & Shectman, S. A. 1988, AJ, 95, 985
- Dressler, A., & Gunn, J. E. 1988, in Large Scale Structures of the Universe, IAU Symp. No.130, eds. J. Audouze *et al.* (Kluwer, Dordrecht), p. 311
- Durret, F., Adami, C., & Lobo, C. 2002, A&A, 393, 439
- Durret, F., Gerbal, D., Lobo, C., & Pichon, C. 1999, A&A, 343, 760
- Fan, X.-H. et al. 1996, AJ, 112, 628
- Forman, W. & Jones, C. 1982, ARA&A, 20, 547
- Ferguson, H. C. & Sandage, A. 1991, AJ, 101, 765
- Hausman, M. A. & Ostriker, J. P. 1978, ApJ, 224, 320
- Jones, C., Mandel, E., Schwarz, J., Forman, W., Murray, S. S., & Harnden, F. R. 1979, ApJ, 234, L21
- Kriessler, J. R. & Beers, T. C. 1997, AJ, 113, 80
- Lugger, P. M. 1986, ApJ, 303, 535
- Oegerle, W. R., Ernst, R. M., & Hoessel, J. G. 1986, AJ, 91, 697

- Oegerle, W. R. & Hill, J. M. 2001, *AJ*, 122, 2858
- Paolillo, M., Andreon, S., Longo, G., Puddu, E., Gal, R. R., Scaramella, R., Djorgovski, S. G., & de Carvalho, R. 2001, *A&A*, 367, 59
- Pelló, R. et al. 1999, *A&A*, 346, 359
- Phillipps, S., Driver, S. P., Couch, W. J., & Smith, R. M. 1998, *ApJ*, 498, L119
- Poggianti, B. M. 2002, *astro-ph/0210233*
- Ritchie, B. W. & Thomas, P. A. 2002, *MNRAS*, 329, 675
- Schechter, P. 1976, *ApJ*, 203, 297
- Schindler, S. & Mueller, E. 1993, *A&A*, 272, 137
- Schindler, S. 2001, *astro-ph/0109040*
- Stoughton, C. et al. 2002, *AJ*, 123, 485
- Takizawa, M. 2000, *ApJ*, 532, 183
- Tomita, A., Nakamura, F. E., Takata, T., Nakanishi, K., Takeuchi, T., Ohta, K., & Yamada, T. 1996, *AJ*, 111, 42
- Trentham, N. & Tully, R. B. 2002, *MNRAS*, 335, 712
- Ulmer, M. P., Wirth, G. D., & Kowalski, M. P. 1992, *ApJ*, 397, 430
- Xia, L. et al. 2002, *PASP*, 114, 1349
- Yuan, Q., Zhou, X., Chen, J., Jiang, Z., Ma, J., Wu, H., Xue, S., & Zhu, J. 2001, *AJ*, 122, 1718
- Yuan et al. 2003, *ApJS* accepted (*astro-ph/0306352*)
- Zhou, X., Chen, J., Xu, W., Zhang, M., Jiang, Z., Zheng, Z., & Zhu, J. 1999, *PASP*, 111, 909
- Zhou, X., Jiang, Z., Xue, S., Wu, H., Ma, J., & Chen, J. 2001, *Chinese Journal of Astronomy and Astrophysics*, 1, 372
- Zhou, X. et al. 2003, *A&A*, 397, 361

Table 1: Parameters of the BATC filters and the statistics of observations of Abell 168.

No.	Filter	$\lambda_{\text{eff}}$ (Å)	FWHM (Å)	Exposure (hours)	$N_1^{\text{a}}$	Seeing <sup>b</sup> (arcsec)	$N_2^{\text{c}}$
(1)	(2)	(3)	(4)	(5)	(6)	(7)	(8)
1	<i>c</i>	4210	309	3.67	11	5.08	1
2	<i>d</i>	4546	332	5.33	16	4.09	1
3	<i>e</i>	4872	374	4.00	12	3.94	2
4	<i>f</i>	5250	344	3.47	11	4.18	4
5	<i>g</i>	5785	289	1.33	4	3.81	0
6	<i>h</i>	6075	308	1.00	3	4.80	3
7	<i>i</i>	6710	491	1.08	4	3.80	3
8	<i>j</i>	7010	238	2.00	6	3.94	1
9	<i>k</i>	7530	192	2.00	6	4.49	3
10	<i>m</i>	8000	255	5.67	17	3.94	1
11	<i>n</i>	8510	167	2.67	8	4.81	2
12	<i>o</i>	9170	247	1.33	4	6.29	1
13	<i>p</i>	9720	275	3.40	11	5.03	2

<sup>a</sup>Number of images of each color.

<sup>b</sup>The seeing is of the combined images.

<sup>c</sup>Number of the calibration images.

Table 2: Parameters of Abell 168.<sup>†</sup>

Parameter	A168N	A168S	A168WG	A168
$N_{\text{gal}}^{\text{a}}$	79	97	19	376
$N_{\text{gal, spec}}^{\text{b}}$	26	52	6	121
$z$	$0.0446 \pm 0.0004$	$0.0455 \pm 0.0003$	$0.0466 \pm 0.0001$	$0.0451 \pm 0.0002$
$v_{\text{r}}$ (km s <sup>−1</sup> )	$13065 \pm 113$	$13329 \pm 86$	$13633 \pm 35$	$13206 \pm 50$
$\sigma_{\text{r}}$ (km s <sup>−1</sup> )	$564 \pm 90$	$613 \pm 56$	$491 \pm 189$	$554 \pm 34$
$\langle 1/r_{\text{p}} \rangle^{-1}$ (Mpc) <sup>c</sup>	0.30	0.30	—	0.77
$M$ ( $10^{14} M_{\odot}$ )	$2.1 \pm 0.7$	$2.5 \pm 0.5$	—	$5.2 \pm 0.6$
AI <sup>d</sup>	−0.263	−0.392	−0.327	−0.093
TI <sup>e</sup>	1.458	0.958	0.000	0.901

<sup>†</sup>The errors are computed at 68% confidence level.

<sup>a</sup>The number of galaxies including the spectroscopically confirmed members and the photometric redshift selected candidates.

<sup>b</sup>The number of galaxies only including the spectroscopically confirmed members.

<sup>c</sup>The gravitational scale length.

<sup>d</sup>Asymmetry index.

<sup>e</sup>Tail index.

Table 3: The fitting results of LF’s of Abell 168. <sup>†</sup>

	$\phi_0^*$	$M_0^*$	$\alpha_0$	$\phi_1^*$	$M_1^*$	$\alpha_1$	$\chi_{\min}^2$
A168N	$14.9^{+3.4}_{-2.9}$	$-21.75^{+0.67}_{-2.50}$	$0.04^{+0.08}_{-0.07}$	$37.5^{+20.2}_{-15.9}$	$-16.91^{+0.56}_{-0.63}$	$0.40^{+0.98}_{-1.00}$	1.6
A168S	$54.4^{+8.5}_{-7.4}$	$-20.47^{+0.31}_{-0.40}$	$0.36^{+0.08}_{-0.08}$	0.00	—	—	3.4
A168N+S	$50.3^{+5.6}_{-5.2}$	$-21.14^{+0.32}_{-0.48}$	$0.05^{+0.04}_{-0.04}$	0.00	—	—	4.1
Total	$95.8^{+10.}_{-9.4}$	$-20.77^{+0.23}_{-0.30}$	$0.17^{+0.05}_{-0.05}$	$138.9^{+24.5}_{-22.6}$	$-17.48^{+0.19}_{-0.20}$	$-0.19^{+0.28}_{-0.26}$	3.6

<sup>†</sup>The errors are computed at 68% confidence level.

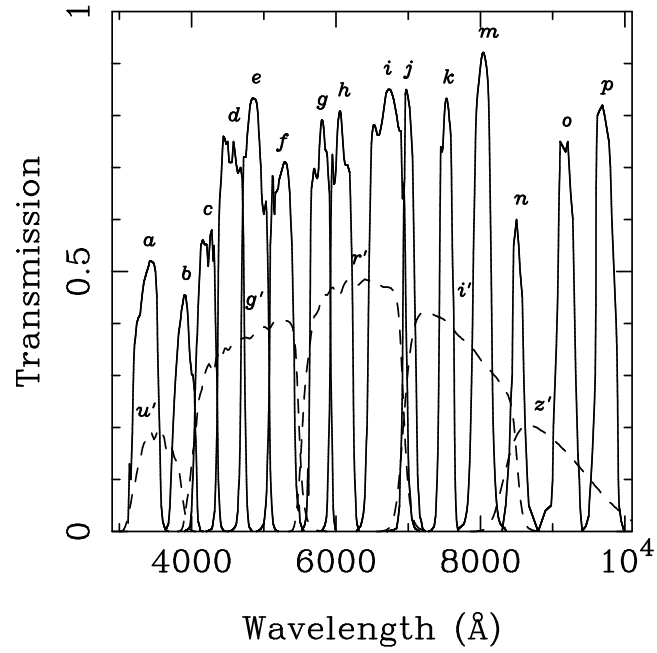


Fig. 1.— The transmission curves of filters in the BATC (solid lines) and the SDSS (dashed lines) photometric system. The names of the filters are marked at the top of each curve.

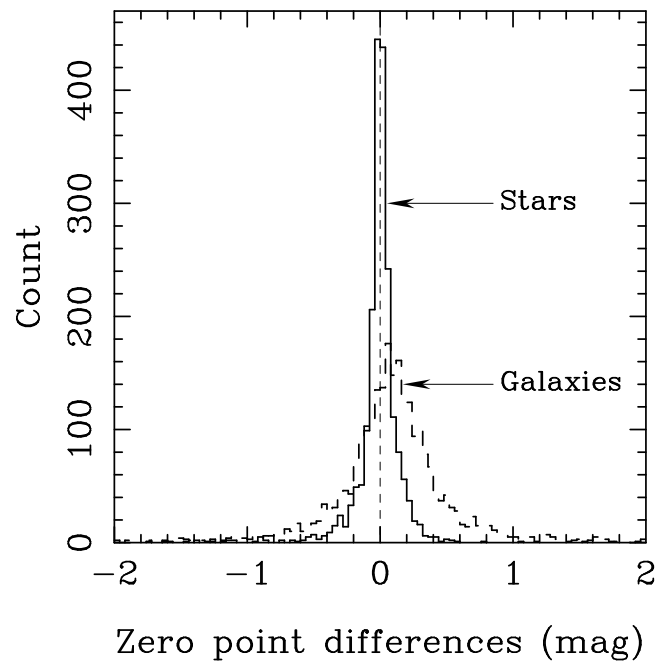


Fig. 2.— The histogram of the zero point differences of individual SEDs in the BATC and the SDSS system for all galaxies and stars.

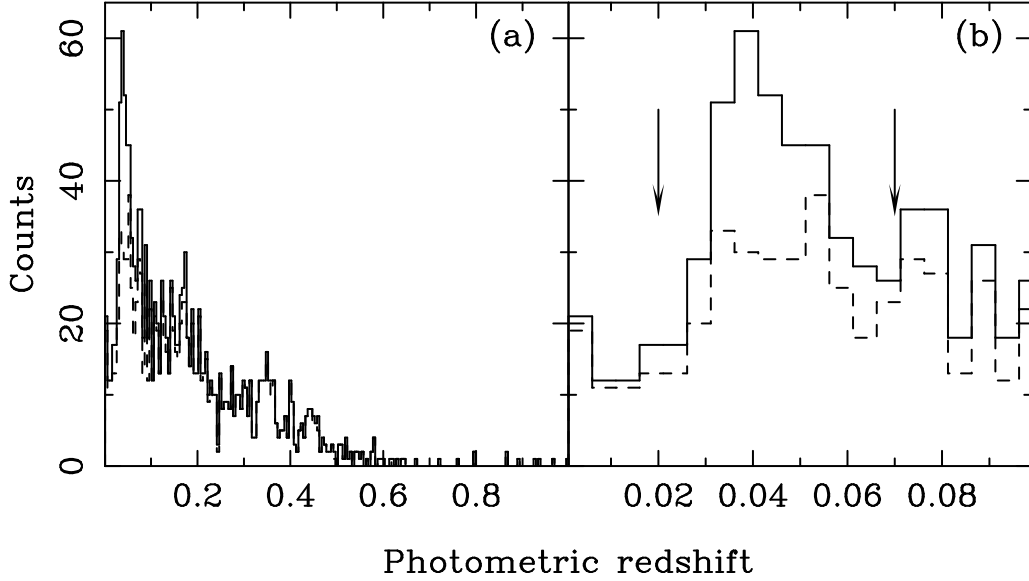


Fig. 3.— Panel (a) shows the histogram of photometric redshift for 1553 galaxies. The distribution from 0.0 to 0.1 is shown enlarged in panel (b). In both figures, the solid lines represent photometric redshifts of all galaxies, the dashed lines indicate photometric redshifts of the galaxies without spectroscopic redshift. The range of  $[0.02, 0.07]$  marked by two arrows is taken as the criterion for member candidates.

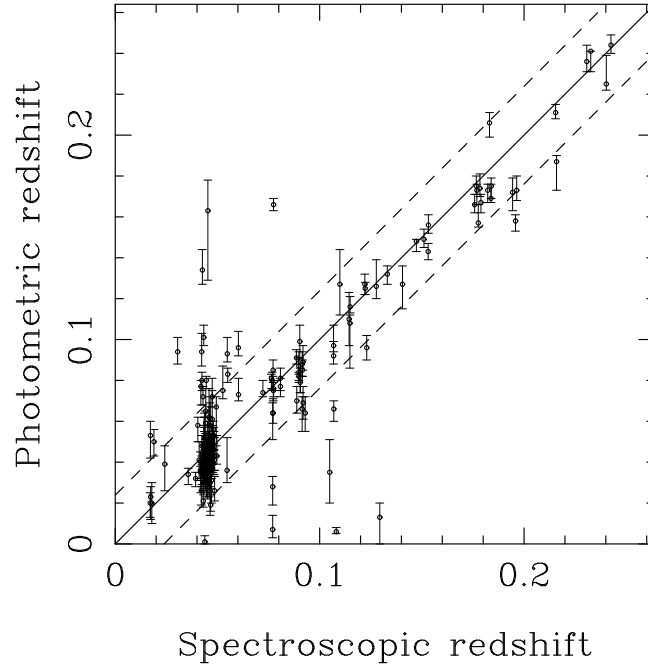


Fig. 4.— A comparison of photometric redshifts and spectroscopic redshifts for 195 known galaxies. The dashed lines mark out the two-sigma region of the photometric redshifts.

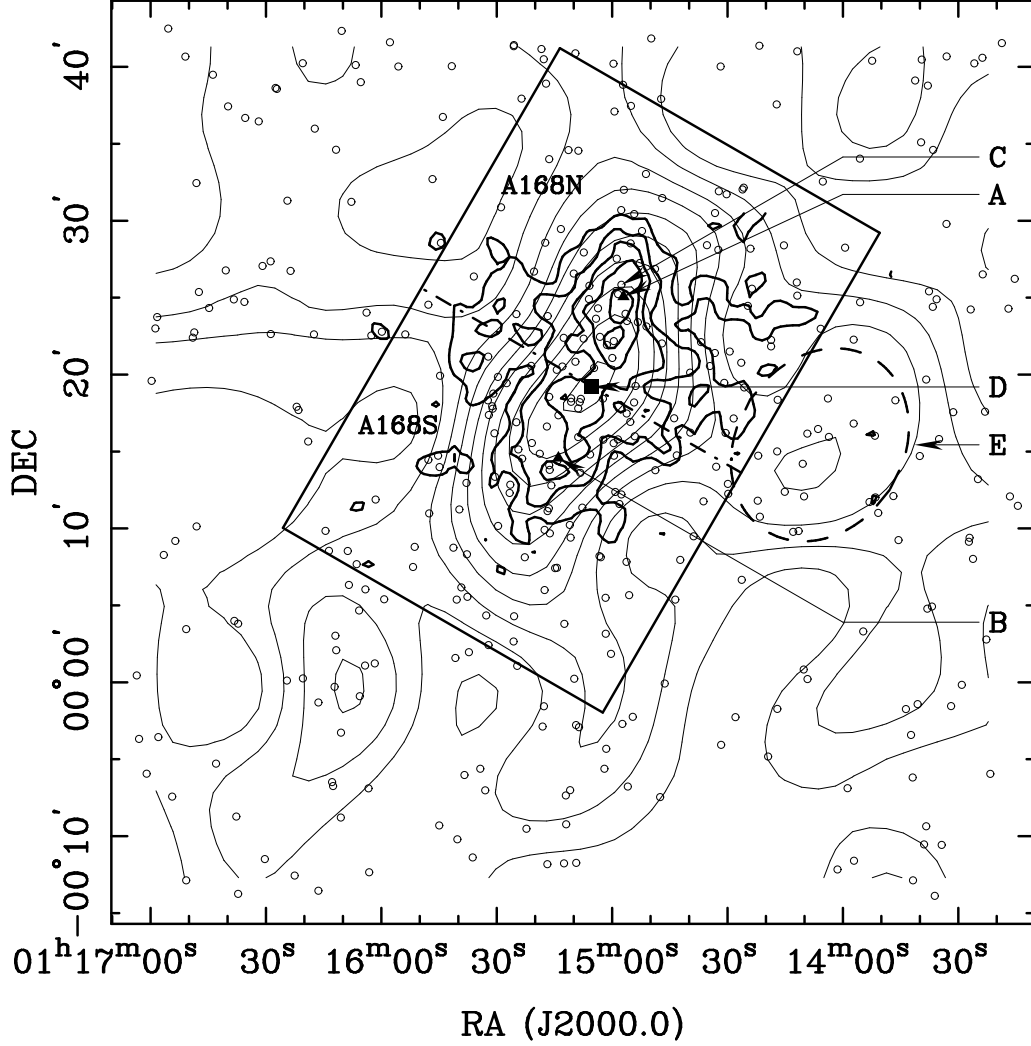


Fig. 5.— Member distribution (small circles) of Abell 168, with corresponding contour map superimposed (thin lines). Point A and point B are the two X-ray peaks. C points to the cD galaxy UGC 00797. D points to the number density peak. E points to the possible west group indicated by a dashed line ellipse. The box ( $0.4^\circ \times 0.6^\circ$ ) indicates the central region of the cluster. The dotted-dashed line divides the north subcluster (A168N) and the south subcluster (A168S) equally (see §3 for detailed analysis).

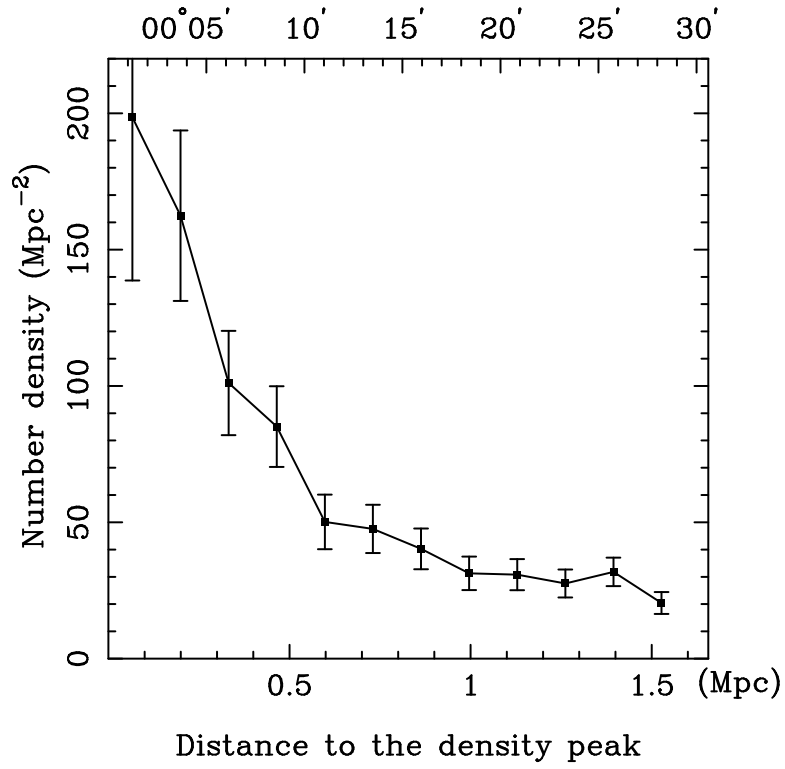


Fig. 6.— The radial number density profile. The bottom abscissa shows the distance in unit of Mpc. The top abscissa is in unit of arcmin.

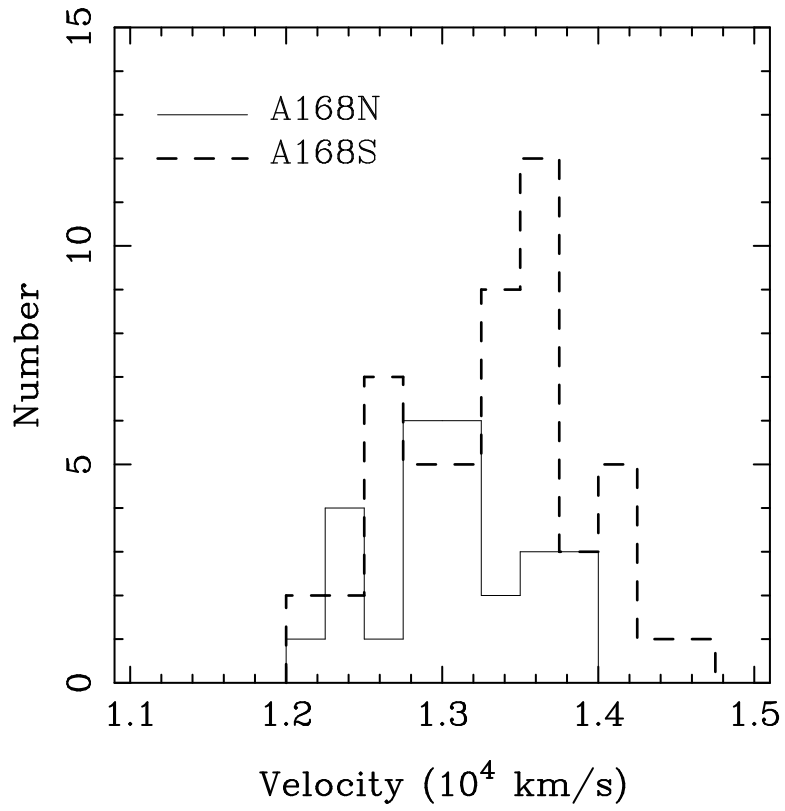


Fig. 7.— The velocity distributions of the spectroscopically confirmed member galaxies for A168N and A168S are presented by the solid line and the dashed line, respectively.

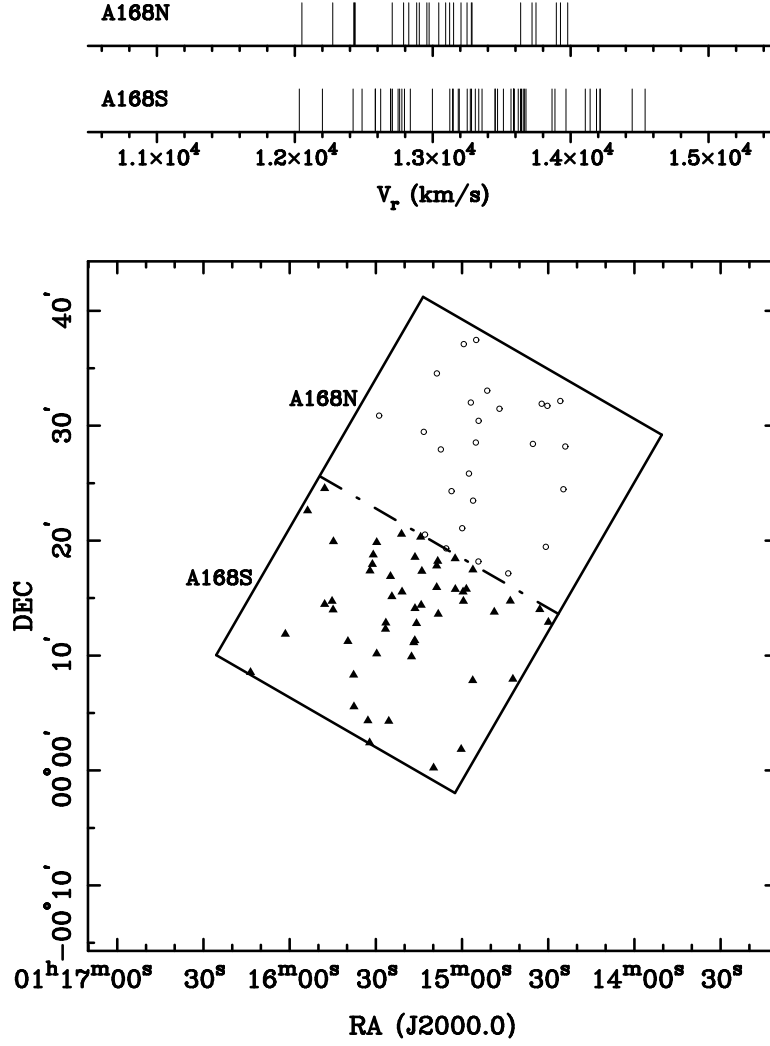


Fig. 8.— For the spectroscopically confirmed members in these two subclusters, the stripe density plot of velocity is plotted above the spatial distribution.

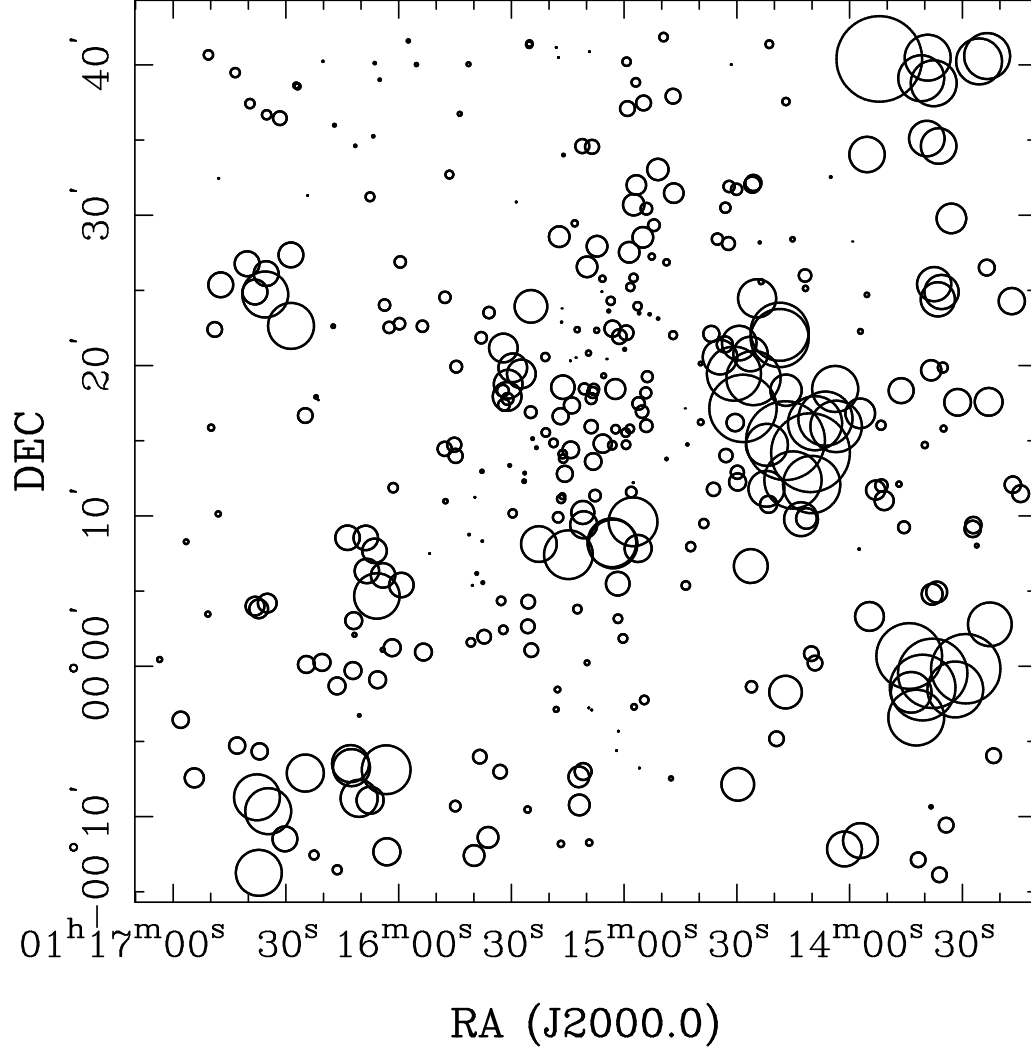


Fig. 9.— The bubble plot shows the deviation of the local velocity distribution for groups of 10 nearest neighbors from the overall velocity distribution. By involving  $10^5$  simulations the significance of existence of substructures reaches  $P(\kappa_{10} > \kappa_{10}^{\text{obs}}) = 0.000\%$ .

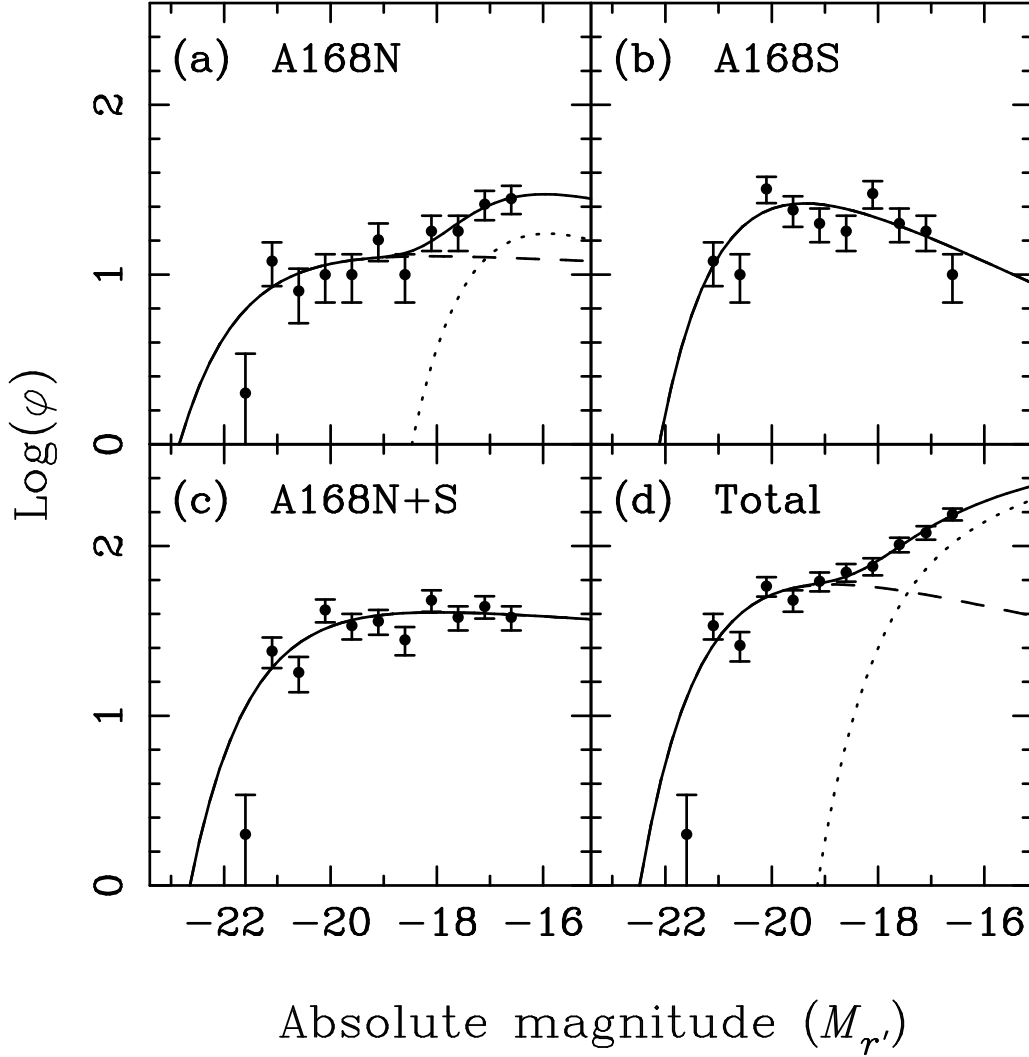


Fig. 10.— The observed luminosity functions are fitted by DSF. The dashed lines and the dotted lines indicate the components of DSF and the solid lines are the sum of them. Panel (a) and (b) are of the north subcluster and south subcluster, respectively. The LF of the central region is plotted in (c). In panel (d) we show the LF of all 376 members in the whole field. For A168S and A168N+S (equal to the central region of Abell 168), the single Schechter function gives a better representation than DSF. The detailed discussion on LFs is made in §4.2.